





RESEARCH ARTICLE

Separations: Materials, Devices and Processes

Optimizing the cask effect in multicomponent natural gas purification to provide high methane productivity

Yuxin Chen¹  | Yunjia Jiang¹ | Jiahao Li¹ | Xianghao Hong¹ | Haofei Ni¹ |
Lingyao Wang¹ | Nan Ma² | Mingman Tong²  | Rajamani Krishna³  |
Yuanbin Zhang¹ 

¹Key Laboratory of the Ministry of Education for Advanced Catalysis Materials, College of Chemistry and Materials Science, Zhejiang Normal University, Jinhua, China

²School of Chemistry and Materials Science, Jiangsu Normal University, Xuzhou, China

³Van't Hoff Institute for Molecular Sciences, University of Amsterdam, Amsterdam, Netherlands

Correspondence

Yuanbin Zhang, Key Laboratory of the Ministry of Education for Advanced Catalysis Materials, College of Chemistry and Materials Science, Zhejiang Normal University, Jinhua 321004, China.

Email: ybzhang@zjnu.edu.cn

Mingman Tong, School of Chemistry and Materials Science, Jiangsu Normal University, Xuzhou 221116, China.

Email: tongmm@jnsu.edu.cn

Funding information

National Natural Science Foundation of China, Grant/Award Numbers: 22378369, 22205207, 22278197, 21908193; Jinhua Industrial Key Project, Grant/Award Number: 2021-1-088

Abstract

The efficient separation of CH₄ from natural gas containing C₂H₆ and C₃H₈ impurities is an important topic. Previous work on the separation of CH₄/C₂H₆/C₃H₈ mixtures often focuses on the C₃H₈/CH₄ selectivity, inadvertently sidelining the critical importance of C₂H₆/CH₄ selectivity. This oversight results in reduced CH₄ productivity and compromised separation efficiency, a phenomenon often termed as the “cask effect.” Herein, we fine-tune the interrelationship between thermodynamics and kinetics, targeting enhanced CH₄ production. A synergistic thermodynamic-kinetic C₃H₈/CH₄ and C₂H₆/CH₄ selectivity is achieved using dynamic breakthrough experiments, underpinned by the stable metal-organic framework TIFSIX-Cu-TPA. The CH₄ productivity in TIFSIX-Cu-TPA is up to 5 mmol g⁻¹, surpassing most of the popular materials. Detailed density functional theory and molecular dynamics computational insights reveal a counteractive thermodynamic-kinetic relationship, proving pivotal for the simultaneous breakthrough of C₂H₆ and C₃H₈ under optimal conditions. Moreover, precise adsorption sites of C₂H₆ and C₃H₈ are clearly determined through in situ single-crystal structures.

KEYWORDS

cask effect, kinetic effect, metal-organic framework, multicomponent separation, natural gas purification

1 | INTRODUCTION

Natural gas, comprising mainly of methane (CH₄), is a widely utilized energy source that presents several benefits, including low cost, eco-friendliness, and abundance in nature.¹⁻³ In addition to CH₄, impurities like ethane (C₂H₆, ~10%), propane (C₃H₈, ~5%), and traces of carbon dioxide (CO₂) exist in the crude stream and impair its combustion quality.⁴ Besides, C₂H₆ and C₃H₈ can be employed to produce ethylene (C₂H₄) and propylene (C₃H₆) if recovered from natural gas, which are the raw materials for various chemicals and polymers.⁵

Amid the techniques employed in industries to separate light hydrocarbons, cryogenic distillation is the dominant separation technology relying on the volatility difference of individual constituents, whereas the process consumes a substantial amount of energy.⁶ Therefore, there is an urgent demand to develop advanced technologies to separate CH₄ from natural gas with high efficiency.

Adsorptive separation using porous solid materials under gentle operating conditions presents a more energy-efficient and economically viable alternative for light hydrocarbon separations, provided that the adsorbents exhibit superb selectivity and capacity for the desired guest molecules as well as sufficient stability.⁷⁻²⁰ Emerging as a prominent class of porous crystalline materials, metal-organic

Yuxin Chen, Yunjia Jiang, and Jiahao Li contributed equally to this study.

frameworks (MOFs) have shown impressive potential for gas separation and purification, beneficial from their high porosity, adjustable and consistent pore dimensions, and manageable surface chemistry.^{21–59} However, previous studies mainly focused on the separation of two-component gas mixtures. When it comes to multicomponent separation, the “cask effect” becomes a non-negligible factor.⁶⁰ Namely, the target gas productivity is determined mainly by the less adsorbed impurity. In NG purification, C₂H₆ usually has lower capacity and selectivity over CH₄ when compared to those of C₃H₈. This shifts the focus to C₂H₆/CH₄ selectivity rather than C₃H₈/CH₄. However, prior MOF-focused studies skewed towards C₃H₈/CH₄ selectivity, often at the expense of actual CH₄ productivity. For example, BSF-1 displays a C₃H₈/CH₄ selectivity of 353 at 298 K, yet its CH₄ productivity languishes at 2.7 mmol g⁻¹ in experimental breakthrough experiments.⁶¹ In BSF-2, the C₃H₈/CH₄ selectivity is even higher, reaching 2609, but CH₄ productivity is reduced to 1.23 mmol g⁻¹ due to the decreased C₂H₆ capacity.⁶² Recently, Li's group reported a series of Al-MOFs for separation of C₃H₈/C₂H₆/CH₄.⁶³ Among them, MOF-303 shines with a C₃H₈/CH₄ selectivity of 5114 but stumbles with a modest C₂H₆/CH₄ selectivity of 20. Such selectivity difference has a strong negative influence on practical dynamic breakthrough results, as shown in Scheme 1A. The valid period for CH₄ purification, namely the area highlighted in blue, occupies only a small area, while the time between the breakthrough of C₂H₆ and C₃H₈ (invalid period) is very long, causing the waste of efficiency. Based on this, we expect that the breakthrough time of C₂H₆ moves afterward and the breakthrough time of C₃H₈ moves forward, thus improving the efficiency in the adsorption circle (Scheme 1B). To reach this point, MOFs with high C₂H₆ capacity and comparable C₂H₆/CH₄ and C₃H₈/CH₄ selectivity are preferred, which can show the enhanced separation performance and efficiency when C₂H₆ and C₃H₈ breakthrough similarly or even simultaneously. Materials based on this strategy, however, have not been reported to the best of our knowledge. Besides, the stability of the MOF adsorbent holds significant importance, as it is a crucial factor for practical implementation. Many preceding materials that exhibit superb separation capabilities often lack stability, with some even displaying sensitivity to moist air.¹⁴

Herein, we reported a chemically stable MOF, TIFSIX-Cu-TPA, using the above strategy focusing on C₂H₆/CH₄ selectivity while subtly moderating C₃H₈/C₂H₆ selectivity (Scheme 1B) to amplify NG purification efficacy. A high productivity of high-purity CH₄ (5 mmol g⁻¹) in breakthrough experiments is achieved. Powder x-ray diffraction (PXRD) data confirmed TIFSIX-Cu-TPA's resilience against

humidity and water, while its thermogravimetric analysis (TGA) profile underscored a commendable thermal stability beyond 300°C. Single-component adsorption isotherms showed that the capacities of CH₄, C₂H₆, and C₃H₈ at 298 K and 1.0 bar are 0.68, 4.40, and 4.91 mmol g⁻¹, respectively. The selectivity was calculated through ideal adsorbed solution theory (IAST), revealing high IAST selectivity of C₃H₈/CH₄ (79) and C₂H₆/CH₄ (16). Such values contribute to similar breakthrough times of C₂H₆ and C₃H₈ by considering the diffusion difference of C₂H₆ and C₃H₈, which greatly improved the productivity and efficiency of CH₄ purification. Subsequently, binding energy and binding sites were studied by density functional theory (DFT) calculations and in situ single-crystal analysis, clearly revealing the thermodynamic adsorption difference for the three alkane molecules. Moreover, molecular dynamics (MD) simulations showed the distinct diffusion rates of C₃H₈, C₂H₆, and CH₄, which confirms the kinetic effects in C₃H₈/C₂H₆/CH₄ separation by TIFSIX-Cu-TPA.

2 | EXPERIMENTAL SECTION

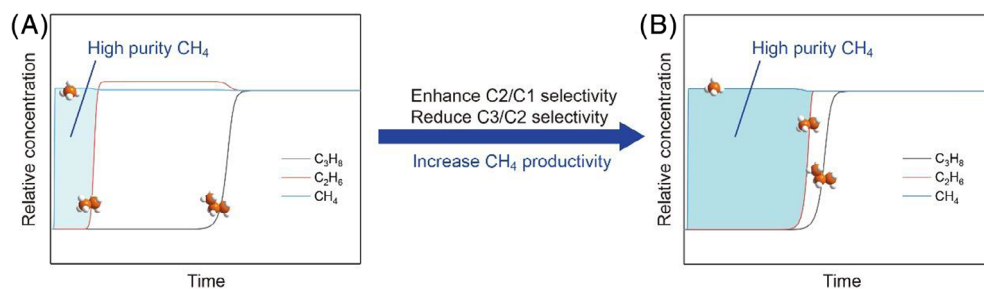
Unless specifically indicated, reactions were conducted under atmospheric conditions, eschewing the use of inert gases such as N₂ or Ar. All reagents were utilized as supplied, without any additional purification, unless otherwise mentioned.

2.1 | Reagents

Tri(pyridine-4-yl)amine (TPA; 99%) was sourced from Tensus Biotech Company and was used without any subsequent purification. The organic compound's purity was ascertained using both ¹H NMR and ¹³C[¹H] NMR spectroscopy. Cu(NO₃)₂·3H₂O (99%) and (NH₄)₂TiF₆ (98%) were procured from Energy Chemical and Alab Chemical, respectively, with both being used without further purification.

2.2 | Preparation of TIFSIX-Cu-TPA crystals

Single crystals of TIFSIX-Cu-TPA were synthesized following the procedure delineated in the referenced literature.⁶⁴ The bulky synthesis of TIFSIX-Cu-TPA crystalline powders is described as follows: TPA (100 mg, 0.4 mmol), Cu(NO₃)₂·3H₂O (73 mg, 0.3 mmol) and (NH₄)₂TiF₆ (68 mg, 0.3 mmol) were combined in a 50 mL round-bottom flask. This mixture was subsequently diluted with 15 mL



SCHEME 1 Schematic illustration of enhancing CH₄ productivity by optimizing the cask effect.

MeOH and 3 mL H₂O. The solution was heated to 348 K and maintained for a period of 72 h. Following this, the resultant purple crystalline powders were separated using filtration, rinsed with H₂O (10 mL × 3) and MeOH (20 mL × 3). The collected product exceeded 175 mg in weight, which, upon complete activation, reduced to approximately 108 mg, corresponding to a yield of about 65%.

2.3 | Powder x-ray diffraction

PXRD data was acquired utilizing a SHIMADZU XRD-6000 diffractometer equipped with a Cu-K α source ($\lambda = 1.540598 \text{ \AA}$). The operational parameters were set at 40 kV and 30 mA, scanning at a rate of $4.0^\circ \text{ min}^{-1}$ over a 2θ range of $5\text{--}50^\circ$.

2.4 | Single-crystal x-ray diffraction

Examinations via single-crystal x-ray diffractions were undertaken on the BrukerAXS D8 VENTURE diffractometer, outfitted with a PHOTON-II detector (MoK α , $\lambda = 0.71073 \text{ \AA}$). The processes of indexing, data integration, and reduction were executed using APEX3. Data and SaintPlus 6.01, respectively. Absorption corrections were achieved via the multi-scan method in SADABS. The crystallographic space group was identified with XPREP in the APEX3 suite. Structural elucidation was done using SHELXS-97, with refinement based on the nonlinear least-squares method on F², in tandem with SHELXL-97, encapsulated within APEX3, WinGX v1.70.01, and OLEX2 v1.1.5. All non-hydrogen atomic positions were anisotropically refined. Disordered stemming from solvent molecules was addressed as diffuse scatter using Platon's Squeeze routine.

2.5 | Thermalgravimetric analysis

TGA was conducted on the TGA STA449F5 apparatus. Assays were performed in a platinum crucible under a nitrogen atmosphere, maintained at a flow rate of 60 mL min^{-1} . Data collection spanned a temperature domain of $50\text{--}600^\circ\text{C}$, increasing at a consistent rate of $10^\circ\text{C min}^{-1}$.

2.6 | Breakthrough experiments

These experiments employed the HPMC-41 (Xuzhou) dynamic gas breakthrough system. Trials used a stainless-steel column (dimensions: $4.6 \text{ mm inner diameter} \times 50 \text{ mm length}$) containing 0.55 g of TIFSIX-Cu-TPA. Activation of the column was achieved by heating to 75°C for 2 h under vacuum conditions, followed by an elevation to 120°C and sustained overnight. Subsequently, a mixed gas of CH₄/C₂H₆/C₃H₈ (85:10:5, vol/vol/vol) was introduced. The outlet gas composition was monitored via gas chromatography on a GC-9860-5CNJ instrument, leveraging a thermal conductivity detector TCD.

Post-breakthrough, samples were regenerated using an Ar flow of 5 mL min^{-1} at 100°C for a duration of 5 h.

2.7 | Gas adsorption measurements

Gas adsorption determinations were executed on a Builder SSA 7000 (Beijing) instrument. Before these measurements, the TIFSIX-Cu-TPA sample was evacuated initially at 25°C for 2 h, followed by 120°C for 10 h, until a vacuum value below $7 \text{ }\mu\text{mHg}$ was achieved. The sorption isotherms were then recorded at 278 K, 298 K, and 308 K on these activated samples. Precise temperature control during experiments was maintained via a water bath ranging from 278 K to 308 K.

2.8 | Unary isotherm data fitting

At three distinct temperatures, 278 K, 298 K, and 308 K, the unary isotherms of C₃H₈, C₂H₆, and CH₄ in TIFSIX-Cu-TPA were analyzed. The isotherm data for C₃H₈ in TIFSIX-Cu-TPA were adeptly represented using the dual-site Langmuir–Freundlich model:

$$q = \frac{q_{\text{sat,A}} b_A p^{\nu_A}}{1 + b_A p^{\nu_A}} + \frac{q_{\text{sat,B}} b_B p^{\nu_B}}{1 + b_B p^{\nu_B}}, \quad (1)$$

where q denotes the amount adsorbed per mass of the adsorbent (mol kg^{-1}) and P signifies the pressure of the bulk gas in equilibrium with the adsorbed phase (expressed in Pa). The saturation capacities of Sites A and B are characterized by parameters $q_{\text{sat,A}}$ and $q_{\text{sat,B}}$, respectively (mol kg^{-1}), and b_A and b_B represent the affinity coefficients for these sites (Pa^{-1}).

The temperature-dependence of the Langmuir–Freundlich parameters from Equation (1) is depicted as:

$$b_A = b_{A0} \exp\left(\frac{E_A}{RT}\right); \quad b_B = b_{B0} \exp\left(\frac{E_B}{RT}\right). \quad (2)$$

In this equation, E_A, E_B are the energy parameters corresponding to Sites A and B.

The isotherms of C₂H₆ seamlessly align with the dual-site Langmuir model, which features temperature-sensitive Langmuir parameters:

$$q = \frac{q_{\text{sat,A}} b_A p}{1 + b_A p} + \frac{q_{\text{sat,B}} b_B p}{1 + b_B p}; \quad b_A = b_{A0} \exp\left(\frac{E_A}{RT}\right); \quad b_B = b_{B0} \exp\left(\frac{E_B}{RT}\right). \quad (3)$$

The isotherms of CH₄ seamlessly align with the single-site Langmuir model, which features temperature-sensitive Langmuir parameters:

$$q = \frac{q_{\text{sat}} b p}{1 + b p}; \quad b = b_0 \exp\left(\frac{E}{RT}\right). \quad (4)$$

The parameters derived from the unary isotherm fitting for TIFSIX-Cu-TPA can be found in Table S2.

2.9 | Determination of isosteric heat of adsorption

The isosteric heat of adsorption, denoted as Q_{st} , is defined by the equation:

$$Q_{st} = -RT^2 \left(\frac{\partial \ln p}{\partial T} \right)_q \quad (5)$$

Here, the derivative on the right-hand side of Equation (5) is computed at a constant adsorbate loading, q . This derivative was ascertained analytically by integrating Equations (1)–(5).

2.10 | IAST calculations: Adsorption selectivity and uptake capacities

The study focuses on the separation of binary mixtures: 50/50 C_3H_8 (1)/ CH_4 (2), 10/90 C_3H_8 (1)/ CH_4 (2), 50/50 C_2H_6 (1)/ CH_4 (2), and 10/90 C_2H_6 (1)/ CH_4 (2) within TIFSIX-Cu-TPA at 298 K, under varied total pressures. The adsorption selectivity for the separation of these binary mixtures, considering species 1 and 2, is represented by

$$S_{ads} = \frac{q_1/q_2}{p_1/p_2} \quad (6)$$

In this context, q_1 and q_2 specify the molar loadings (units: mol kg^{-1}) in the adsorbed phase, which achieves equilibrium with a gas mixture having partial pressures p_1 and p_2 in the bulk gas.

2.11 | DFT calculations

DFT calculations were executed utilizing the CP2K package (version 2022.1) through the Gaussian plane approach encompassed within the QUICKSTEP module. We opted for the Perdew–Burke–Ernzerhof exchange–correlation functional, incorporating the Grimme–D3 dispersion correction. The study employed both double-zeta valence polarized sets and Goedecker–Teter–Hutter pseudopotentials. Plane-wave and relative cut-offs were designed as 400 and 55 Ry, respectively. The convergence criteria for inner and outer SCF were determined to be 2.0×10^{-6} Ha. All structural geometrical optimizations were undertaken at the Γ point, ensuring the relaxation of all constituent atoms. The thresholds for root mean square and maximum force convergence were defined as 3.0×10^{-4} and 4.5×10^{-4} Ha \AA^{-1} , respectively.

Adsorption energies were determined using the following equation:

$E_{ads} = E_{(\text{MOF} + \text{adsorbate})} - E_{(\text{MOF})} - E_{(\text{adsorbate})}$, where $E_{(\text{MOF} + \text{adsorbate})}$, $E_{(\text{MOF})}$, and $E_{(\text{adsorbate})}$ where the respective terms represent the electronic energies of the adsorbate-bound MOF, the isolated MOF, and the singular adsorbate molecule.

2.12 | MD simulations

To probe the diffusion characteristics of CH_4 , C_2H_6 , and C_3H_8 in TIFSIX-Cu-TPA, MD simulations in the NVT ensemble were deployed. These simulations were uniformly conducted under conditions of 298 K and 1 bar pressure. Temperature stabilization was ensured via the Nosé–Hoover chain thermostat. Integration of Newton's motion equations was facilitated by the velocity Verlet scheme. The universal force field aptly described van der Waals interactions, with computations limited to a 14 \AA cut-off radius. Atom charge assignments were facilitated by the QEq methodology. Ewald summation served as the evaluation technique for long-range electrostatic interactions. Each simulation ran for 3×10^6 steps, equivalent to 3 ns, following an equilibration phase of 2×10^6 steps (or 2 ns). All computational tasks were executed through the HT-CADSS software suite.

3 | RESULTS AND DISCUSSION

The bulky synthesis of crystalline powders of TIFSIX-Cu-TPA was reported for the first time in this work. Single crystals of TIFSIX-Cu-TPA were synthesized according to our earlier study.⁶⁴ By layering a MeOH solution of TPA onto the $CuTiF_6$ in an aqueous solution, purple single crystals were obtained. X-ray structure analysis revealed that TIFSIX-Cu-TPA crystallizes within the symmetrical cubic space group Pm-3n. The framework is composed of large icosahedral cages and small tetrahedral cages (Figure 1A). Every small cage possesses four windows, interfacing with large cages, while every large cage features 12 windows, communicating with adjacent small cages. As shown in Figure 1B, the calculated size of the cage window is 2.4 \AA . There are abundant Lewis basic F functional sites and aromatic rings on the surface of these cages, which allow the potential strong trap of C_3H_8 and C_2H_6 by multiple host–guest interactions.

The stability of TIFSIX-Cu-TPA was corroborated using TGA and PXRD. As shown in Figure 2A, PXRD patterns of as-synthesized samples match well with stimulated patterns, verifying the high purity of the synthesized material. TIFSIX-Cu-TPA remained stable after immersion in H_2O and exposure to humid air for 6 months, underscoring its pronounced chemical robustness. Moreover, the TGA curve (Figure 2B) demonstrates that TIFSIX-Cu-TPA has good thermal stability of $\sim 308^\circ\text{C}$.

Based on the analysis of the single-crystal structure as well as the previous C_3H_4/C_3H_6 separation investigation,⁶⁴ it is posited that both thermodynamic and kinetic influences significantly contribute to the effective separation of $C_3H_8/C_2H_6/CH_4$, given the compact window size (2.4 \AA ; Figure 1B). Experimental breakthrough experiments were thus conducted on ternary gas mixtures ($CH_4/C_2H_6/C_3H_8$, 85:10:5, vol/vol/vol) under different flow rates at 298 K (Figure S17). With the flow rate of 4 mL min^{-1} (Figure 3A), CH_4 escaped from the adsorption column immediately, followed by C_2H_6 and C_3H_8 , which were detected after 22 and 24 min. As expected, the breakthrough time of C_2H_6 and C_3H_8 is very close, leading to a high CH_4 productivity

FIGURE 1 (A) Overview of TIFSIX-Cu-TPA structure with large cage and small cages. (B) Void surface of TIFSIX-Cu-TPA.

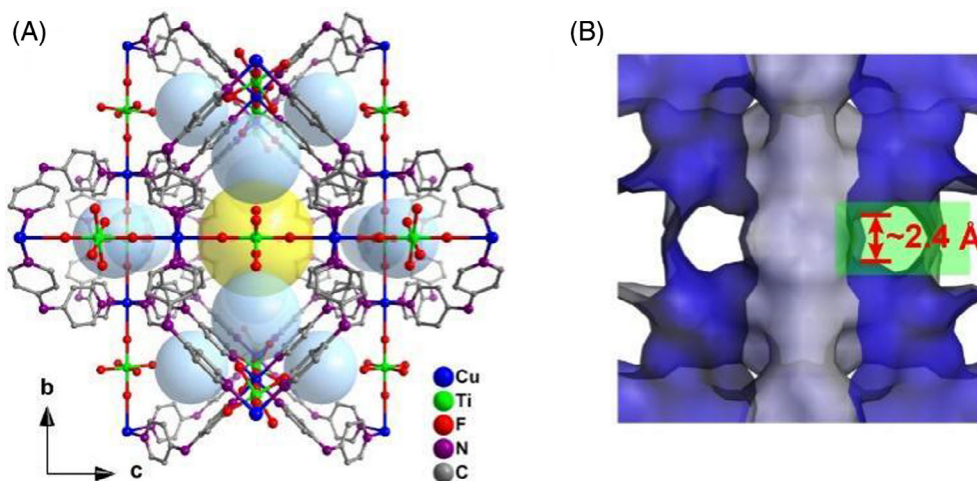
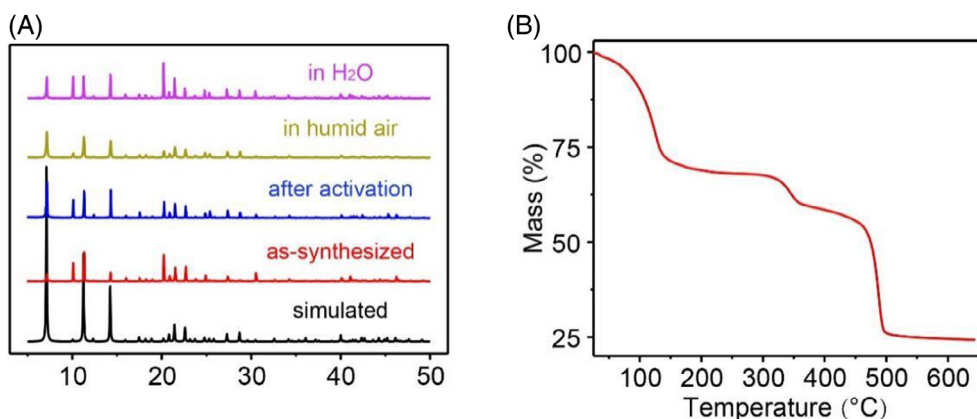


FIGURE 2 (A) Powder x-ray diffraction of TIFSIX-Cu-TPA after different treatments. (B) Thermogravimetric analysis curves of TIFSIX-Cu-TPA.



(5 mol kg⁻¹) and enhanced separation efficiency (4.3 mol kg⁻¹ h⁻¹). The CH₄ productivity is superior to many popular MOFs such as BSF-1 (2.7 mol kg⁻¹),⁶¹ BSF-2 (1.23 mol kg⁻¹),⁶² MOF-801 (1.24 mol kg⁻¹),⁶⁵ MIL-101-Cr (2.42 mol kg⁻¹),⁶⁶ MIL-101-Fe-NH₂ (1.48 mol kg⁻¹),⁶⁶ and so forth (Figure S19). Cyclic breakthrough experiments were carried out next (Figure 3B), revealing the good recycling stability of TIFSIX-Cu-TPA. An experimental breakthrough experiment with a lower flow rate (2 mL min⁻¹) was also conducted. As shown in Figure 3C, C₂H₆ breaks out apparently earlier than C₃H₈, which is quite different from the experiments with the flow rate of 4 mL min⁻¹. The difference can be explained by the fact that more C₃H₈ molecules that are inclined to pass through the gaps between crystals under a fast flow rate can be trapped in the micropores under a slower flow rate, reflecting the slow kinetics of C₃H₈. Breakthrough experiments under humid conditions (RH = 80%) further confirmed that TIFSIX-Cu-TPA remains excellent separation performance under the interference of water vapor (Figure 3D). Besides, as shown in Figure S16, the material can be regenerated within 3 h by Ar purge at 75°C.

In assessing the thermodynamic adsorption disparities, single-component adsorption isotherms of C₃H₈, C₂H₆, and CH₄ were obtained at 278 K, 298 K, and 308 K (Figures S8–S10). Figure 4A–C depicts that the CH₄ adsorption isotherms are quasi-linear with a gas

uptake as low as 0.68 mmol g⁻¹ at 298 K and 1 bar, underscoring TIFSIX-Cu-TPA's limited affinity towards CH₄. As the carbon chain lengthens, the molecule's kinetic diameter and polarizability augment, enhancing the host-guest interactions with the framework. Consequently, the adsorption uptakes of C₂H₆ (4.40 mmol g⁻¹) and C₃H₈ (4.91 mmol g⁻¹) markedly surpass that of CH₄ at the aforementioned conditions. Such proficiency surpasses many renowned porous materials, for example, BSF-2 (1.22 mmol g⁻¹ for C₂H₆ and 1.77 mmol g⁻¹ for C₃H₈)⁶² HOF-ZJU-201a (3.16 mmol g⁻¹ for C₂H₆ and 2.61 mmol g⁻¹ for C₃H₈)⁶⁷ and INOF-1 (4.14 mmol g⁻¹ for C₂H₆ and 4.25 mmol g⁻¹ for C₃H₈),⁶⁸ yet falls short of C-PVDC-800 (5.28 mmol g⁻¹ for C₂H₆ and 5.21 mmol g⁻¹ for C₃H₈)⁶⁹ and JLU-Liu38 (4.96 mmol g⁻¹ for C₂H₆ and 8.39 mmol g⁻¹ for C₃H₈).⁷⁰ While changing the temperatures, the uptakes still remain relatively high. Notably, at 308 K, the adsorption uptakes of C₃H₈ only diminish to 4.70 mmol g⁻¹ at 1 bar and 3.03 mmol g⁻¹ at 0.15 bar (Figure 4C), suggesting TIFSIX-Cu-TPA's robust adsorption capabilities across varying temperatures and pressures. The isosteric heats of adsorption (Q_{st}) of TIFSIX-Cu-TPA were derived via the Clausius-Clapeyron equation. The Q_{st} values at near-zero loading of CH₄, C₂H₆, and C₃H₈ are 18.5, 27.3, and 29.4 kJ mol⁻¹, respectively (Figure 4D), which indicate that the affinity of the framework towards gas molecule follows the order of CH₄ < C₂H₆ < C₃H₈. In addition, the relatively modest

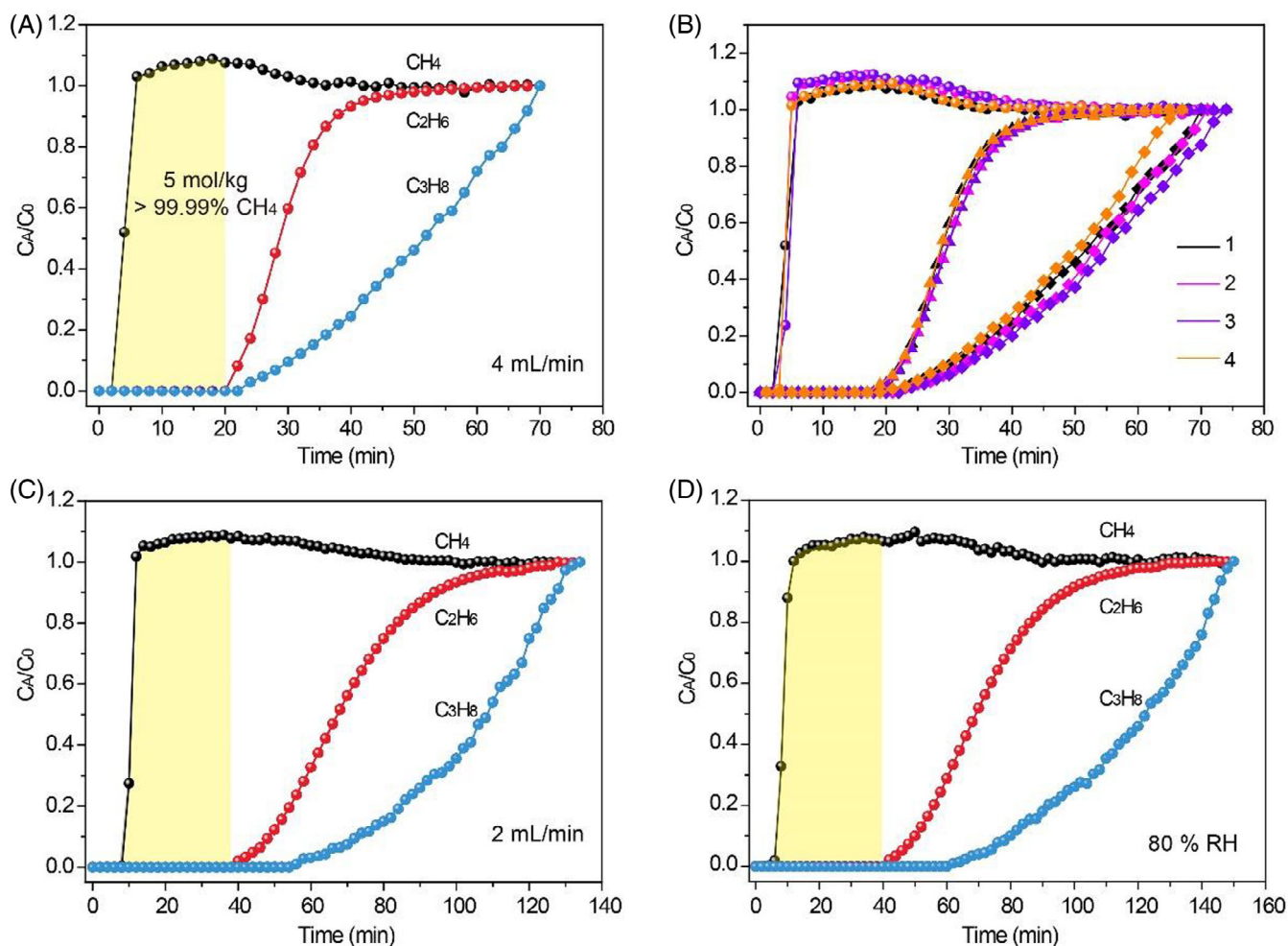


FIGURE 3 (A) Experimental breakthrough curves of TIFSIX-Cu-TPA for $C_3H_8/C_2H_6/CH_4$ (5/10/85) at 298 K with a flow rate of 4 mL min^{-1} . (B) Four cycles of experimental breakthrough curves of TIFSIX-Cu-TPA for $C_3H_8/C_2H_6/CH_4$ (5/10/85) at 298 K (C) Experimental breakthrough curves of TIFSIX-Cu-TPA for $C_3H_8/C_2H_6/CH_4$ (5/10/85) at 298 K with a flow rate of 2 mL min^{-1} . (D) Experimental breakthrough curves of TIFSIX-Cu-TPA for $C_3H_8/C_2H_6/CH_4$ (5/10/85) at 298 K under humid conditions (RH = 80%).

Q_{st} values for C_2H_6 and C_3H_8 (Figure S18) affirm the potential of TIFSIX-Cu-TPA for regeneration under gentle conditions.

The IAST selectivity is another parameter applied to evaluate the separation behaviors of TIFSIX-Cu-TPA. The separation selectivities were calculated after fitting the adsorption isotherms to single-site Langmuir equation (CH_4), dual-site Langmuir equation (C_2H_6) or dual-site Langmuir-Freundlich equations (C_3H_8). The IAST-predicted selectivities for C_2H_6/CH_4 remain stable under the change of pressure or gas ratio (Figure 5A,B). Typically, the value is estimated to be 16.2 at 298 K and 100 kPa for separating equimolar C_2H_6 and CH_4 (Figure 5A), which is lower than some reported materials such as BSF-2 (52)⁶² but still exceeds many adsorbents such as UPC-21 (15.3)⁷¹ and HOF-14 (6.3).⁷² The IAST-predicted selectivity for 50/50 C_3H_8/CH_4 reaches the top value of 78.9 at 22 kPa and gradually decreases to 68.6 at 100 kPa (Figure 5C). For the 10/90 C_3H_8/CH_4 mixture (Figure 5D), the selectivity increases with mounting pressure and reaches 78.9 at 100 kPa. The C_3H_8/CH_4 selectivity of TIFSIX-Cu-TPA surpasses those of many reported porous materials including

HOF-ZJU-202a (40)⁶⁷ and UPC-21 (67),⁷¹ though is not on par with top-tier materials such as BSF-2 (2169)⁶² and MIL-142A (1300).⁷³

To elucidate the specific adsorption sites within TIFSIX-Cu-TPA, in situ single-crystal structures of TIFSIX-Cu-TPA with gas loading were studied. Figure 6A reveals two different binding sites for C_2H_6 : one is located in the large cage, the other is located in the small cage. Each large cage adsorbs 2.2 C_2H_6 molecules, while each small cage adsorbs 0.9 C_2H_6 molecules, equaling 2.5 C_2H_6 molecules per TiF_6^{2-} anion. In small cages, the C_2H_6 molecules interact with F atoms via multiple $H \cdots F$ hydrogen bonds with distances of 2.16, 2.48, and 2.49 Å (Figure 6B). As for C_3H_8 , there is only one binding site in the large cage that can be directly identified. In each large cage, six C_3H_8 molecules are adsorbed, corresponding to two C_3H_8 molecules adsorbed by each TiF_6^{2-} anion (Figures 6C and S11). Specifically, the C_3H_8 molecules interact with the framework via multiple $H \cdots F$ hydrogen bonds with distances of 1.70, 1.82, 2.56, and 2.71 Å (Figure 6D).

To further verify the binding sites and bonding energy from multiple perspectives, DFT calculations were carried out. Figure 7A shows

FIGURE 4 (A) C_3H_8 , C_2H_6 , and CH_4 adsorption isotherms of TIFSIX-Cu-TPA at 278 K. (B) C_3H_8 , C_2H_6 , and CH_4 adsorption isotherms of TIFSIX-Cu-TPA at 298 K. (C) C_3H_8 , C_2H_6 , and CH_4 adsorption isotherms of TIFSIX-Cu-TPA at 308 K. (D) The isosteric heat of adsorption, Q_{st} , for C_3H_8 , C_2H_6 , and CH_4 in TIFSIX-Cu-TPA.

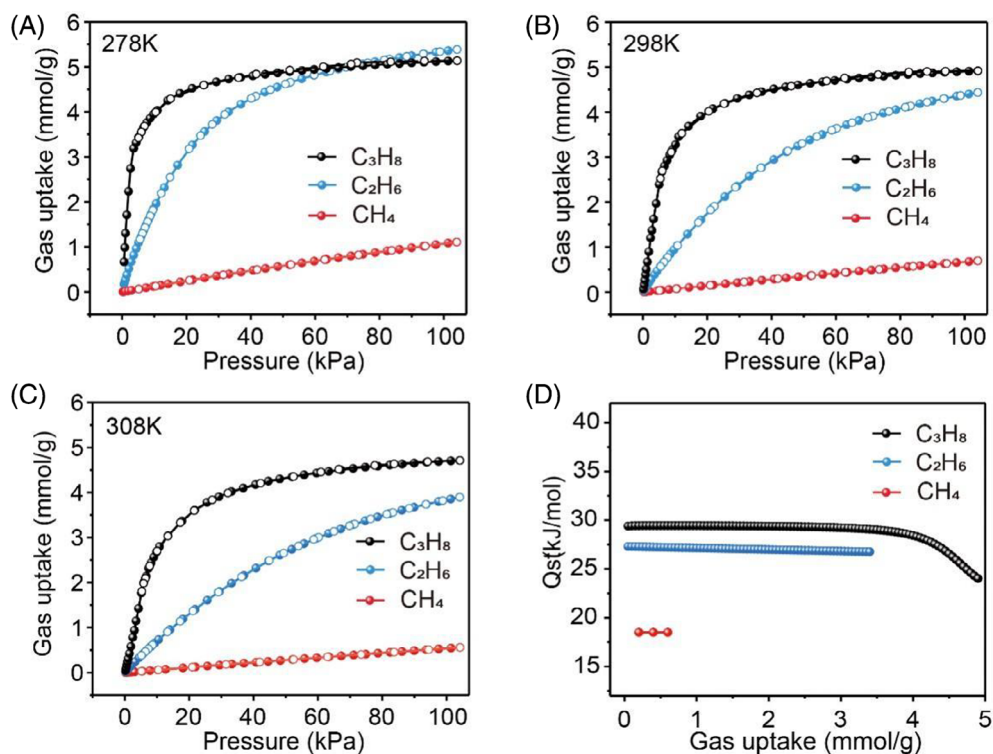
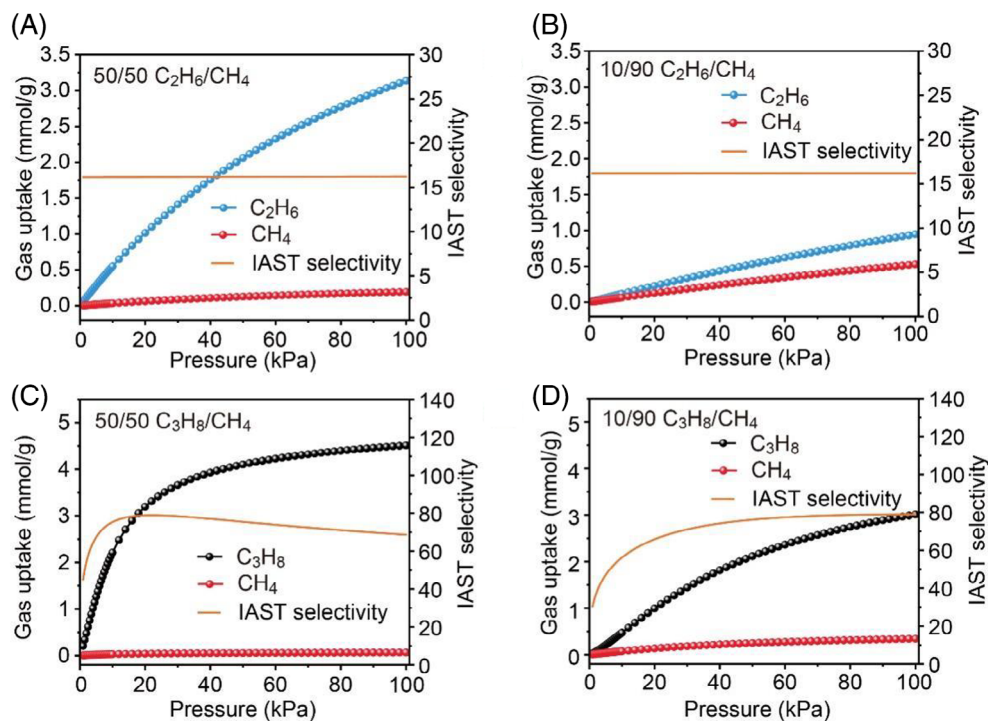


FIGURE 5 (A, B) IAST predicted selectivity and adsorption capacity of 50/50 and 10/90 C_2H_6/CH_4 for TIFSIX-Cu-TPA at 298 K. (C, D) IAST predicted selectivity and adsorption capacity of 50/50 and 10/90 C_3H_8/CH_4 for TIFSIX-Cu-TPA at 298 K.



the contract window is the major adsorption site for CH_4 , where CH_4 is captured via two C··H interactions (2.75 Å) with the binding energy of $-25.0 \text{ kJ mol}^{-1}$. The secondary site for CH_4 adsorption is within the large cage characterized by F··H interactions with the binding energy of $-19.5 \text{ kJ mol}^{-1}$ (Figure S12). For C_2H_6 , several potential sites are explored. The binding energies are higher (-33.2 to $-31.9 \text{ kJ mol}^{-1}$) when C_2H_6 is trapped in the small cage and close to

the window (Figures 7B and S13). In these sites, C_2H_6 was bound to the framework mainly via multiple C··H interactions from the pyridine ring (2.37–2.77 Å). Another site is located in the large cage, capturing C_2H_6 via two strong F··H interactions ($\Delta E = -29.0 \text{ kJ mol}^{-1}$) at distances of 2.37 and 2.54 Å, respectively (Figure 7C). As to the C_3H_8 molecule, the DFT calculation was performed based on the optimization of the in situ C_3H_8 -loaded single-crystal structure.

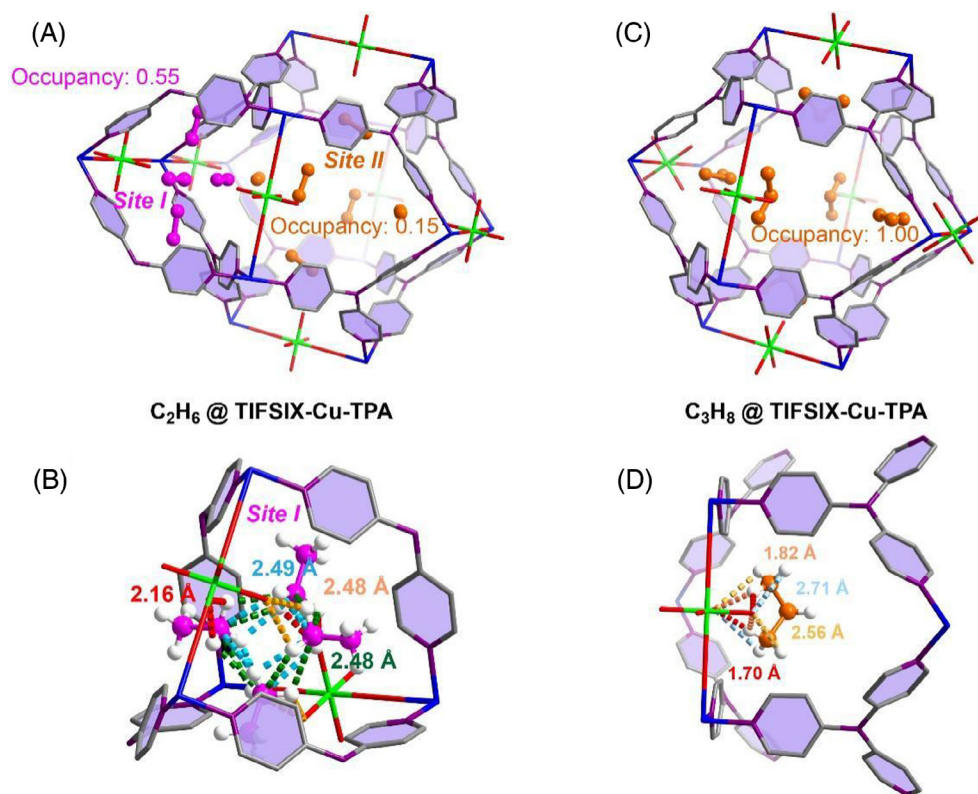


FIGURE 6 Single-crystal structure of gas-loaded TIFSIX-Cu-TPA. (A) A holistic view of $C_2H_6@TIFSIX-Cu-TPA$. (B) Binding Site I of C_2H_6 in the small cage. (C) A holistic view of $C_3H_8@TIFSIX-Cu-TPA$. (D) The binding site of C_3H_8 in the large cage.

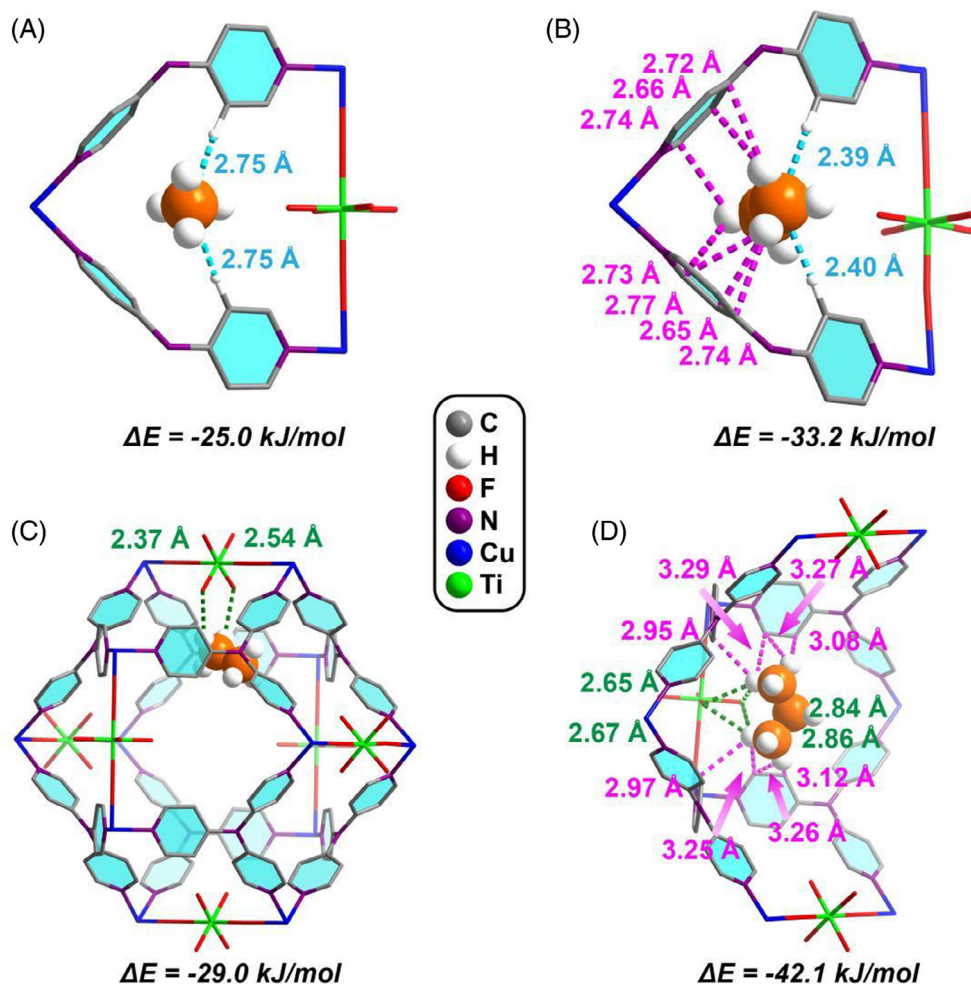


FIGURE 7 The density functional theory optimized gas adsorption configuration. (A) The binding site of CH_4 in the window. (B) The binding site of C_2H_6 inside the small cage. (C) The binding site of C_2H_6 inside the large cage. (D) The binding site of C_3H_8 inside the large cage.

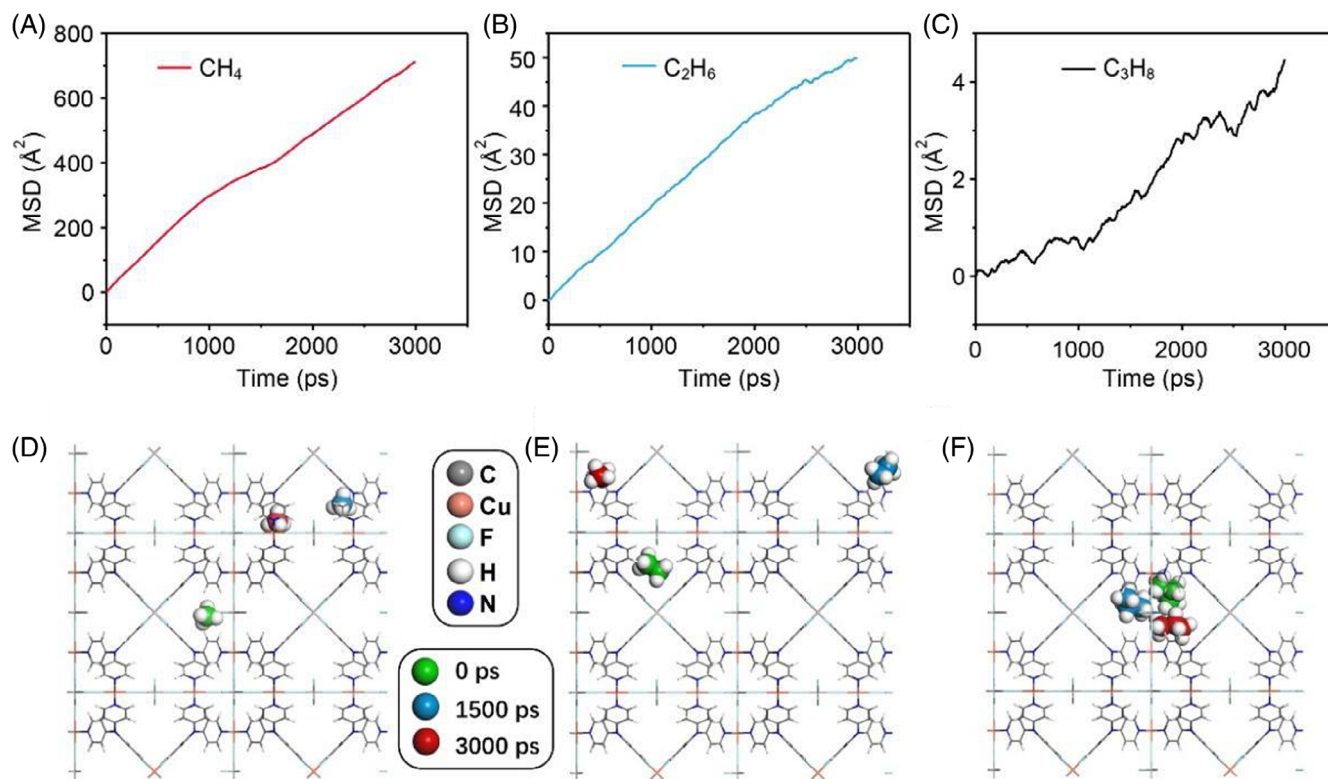


FIGURE 8 Molecular dynamics (MD) simulations. (A–C) Mean square displacement plot of CH₄, C₂H₆, and C₃H₈ molecules in a single cage. (D–F) Snapshots of MD simulation of CH₄ (D), C₂H₆ (E), and C₃H₈ (F) molecules at 0, 1500, and 3000 ps.

As shown in Figure 7D, C₃H₈ is tightly captured via multiple F⋯H hydrogen bonds (2.65–2.86 Å) and multiple H⋯C(Py) interactions, leading to the highest bonding energy of $-41.7 \text{ kJ mol}^{-1}$.

MD simulations were employed to discern the adsorption kinetics for CH₄, C₂H₆, and C₃H₈. Figure 8A–C illustrates the mean square displacement in the x, y, and z directions, respectively, for CH₄, C₂H₆, and C₃H₈ molecules within the framework of TIFSIX-Cu-TPA. Over a span of 3000 ps, C₃H₈ exhibited limited displacement compared to CH₄ and C₂H₆. Based on the data, diffusion coefficients that further reflected diffusion rates of CH₄, C₂H₆, and C₃H₈, were calculated to be 5.15×10^{-10} , 3.06×10^{-11} , and $3.49 \times 10^{-12} \text{ m}^2 \text{ s}^{-1}$, respectively. Figure 8D–F visualizes the diffusion pathways of these molecules. Within 3000 ps, C₃H₈ is restricted in the original cage (Figure 8F), while CH₄ and C₂H₆ are able to migrate freely from the initial cage to other cages (Figure 8D,E), further identifying that C₃H₈ molecules have a low diffusion rate in the framework. Therefore, TIFSIX-Cu-TPA favors C₂H₆ over C₃H₈ kinetically, contrary to the thermodynamic effect. The interplay between thermodynamic and kinetic effects results in TIFSIX-Cu-TPA's optimized performance for practical separation.

4 | CONCLUSIONS

In conclusion, we introduced a chemically stable MOF, TIFSIX-Cu-TPA. By integrating both thermodynamic and kinetic effects, this MOF can efficiently purify CH₄ from natural gas, achieving high

productivity (5 mol kg^{-1}) and commendable efficiency ($4.3 \text{ mol kg}^{-1} \text{ h}^{-1}$). The synergy between C₂H₆/CH₄ and C₃H₈/CH₄ separation has been optimized, resulting in analogous thermodynamic–kinetic selectivities. This, in turn, ensures that C₂H₆ and C₃H₈ are retained within the fixed bed over comparable durations. A thorough investigation into the separation mechanism, incorporating DFT calculations, in situ single-crystal structural analysis, and MD simulations, elucidated the reversed thermodynamic and kinetic orders for C₃H₈, C₂H₆, and CH₄ adsorption. It is worth noting that TIFSIX-Cu-TPA displays high adsorption capacities for C₃H₈ and C₂H₆ with low adsorption heat, facilitating efficient adsorption and desorption processes. Broadly speaking, our findings underscore the potential of enhancing CH₄ productivity by modulating C₂H₆/CH₄ and C₃H₈/CH₄ selectivities to a similar level, thereby augmenting natural gas separation. This approach holds promise for broader applications in multicomponent separations, providing a solution to counterbalance the cask effect.

AUTHOR CONTRIBUTIONS

Yuxin Chen: Conceptualization (lead); data curation (lead). **Yunjia Jiang:** Conceptualization (equal). **Jiahao Li:** Data curation (lead). **Xianghao Hong:** Data curation (supporting). **Haofei Ni:** Data curation (supporting). **Lingyao Wang:** Investigation (supporting); supervision (supporting). **Nan Ma:** Investigation (supporting). **Mingman Tong:** Supervision (equal); writing – original draft (supporting). **Rajamani Krishna:** Investigation (supporting); validation (supporting). **Yuanbin Zhang:** Conceptualization (lead); funding acquisition (lead); visualization (lead); supervision (lead); writing – review and editing (lead).

ACKNOWLEDGMENTS

This study was supported by the National Natural Science Foundation of China (No. 22378369, 22205207, 22278197, and 21908193) and the Jinhua Industrial Key Project (No. 2021-1-088).

DATA AVAILABILITY STATEMENT

The data that support the findings of this study are available from the corresponding author upon reasonable request. The numerical data from Figures 2–5 and 8 are tabulated in the Supplementary Material.

ORCID

Yuxin Chen  <https://orcid.org/0009-0002-1780-0621>

Mingman Tong  <https://orcid.org/0000-0002-9357-5684>

Rajamani Krishna  <https://orcid.org/0000-0002-4784-8530>

Yuanbin Zhang  <https://orcid.org/0000-0002-8268-384X>

REFERENCES

1. He Y, Zhou W, Qian G, Chen B. Methane storage in metal-organic frameworks. *Chem Soc Rev.* 2014;43(16):5657-5678.
2. Makal TA, Li JR, Lu W, Zhou HC. Methane storage in advanced porous materials. *Chem Soc Rev.* 2012;41(23):7761-7779.
3. Sun W, Hu J, Duttwyler S, Wang L, Krishna R, Zhang Y. Highly selective gas separation by two isostructural boron cluster pillared MOFs. *Sep Purif Technol.* 2022;283:120220.
4. Wang SM, Yang QY. A copper-based metal-organic framework for upgrading natural gas through the recovery of C₂H₆ and C₃H₈. *Green Chem Eng.* 2023;4(1):81-87.
5. Guo P, Chang M, Yan T, Li Y, Liu D. A pillared-layer metal-organic framework for efficient separation of C₃H₈/C₂H₆/CH₄ in natural gas. *Chin J Chem Eng.* 2022;42:10-16.
6. Wu H, Gong Q, Olson DH, Li J. Commensurate adsorption of hydrocarbons and alcohols in microporous metal organic frameworks. *Chem Rev.* 2012;112(2):836-868.
7. Sholl DS, Lively RP. Seven chemical separations. *Nature.* 2016;532:435-437.
8. Bereciartua PJ, Cantín Á, Corma A, et al. Control of zeolite framework flexibility and pore topology for separation of ethane and ethylene. *Science.* 2017;358(6366):1068-1071.
9. Lu W, Huang H, Zhu H, et al. Efficient separation of 1,3-butadiene from C₄ hydrocarbons by flexible metal-organic framework with gate-opening effect. *AIChE J.* 2022;68(4):e17568.
10. Wu H, Chen Y, Yuan Y, et al. The modulation of ethane-selective adsorption performance in series of bimetal PCN-250 metal-organic frameworks: impact of metal composition. *AIChE J.* 2022;68(1):e17385.
11. Yang L, Yan L, Wang Y, et al. Adsorption site selective occupation strategy within a metal-organic framework for highly efficient sieving acetylene from carbon dioxide. *Angew Chem Int Ed.* 2021;60(9):4570-4574.
12. Li L, Yang L, Wang J, et al. Highly efficient separation of methane from nitrogen on a squarate-based metal-organic framework. *AIChE J.* 2018;64(10):3681-3689.
13. Qian S, Hu J, Wang X, et al. Anion-pillared microporous material incorporated mixed-matrix fiber adsorbents for removal of trace propyne from propylene. *AIChE J.* 2023;69(7):e18091.
14. O'Nolan D, Kumar A, Zaworotko MJ. Water vapor sorption in hybrid pillared square grid materials. *J Am Chem Soc.* 2017;139(25):8508-8513.
15. Ding Q, Zhang Z, Yu C, et al. Separation of propylene and propane with a microporous metal-organic framework via equilibrium-kinetic synergetic effect. *AIChE J.* 2021;67(1):e17094.
16. Cui X, Chen K, Xing H, et al. Pore chemistry and size control in hybrid porous materials for acetylene capture from ethylene. *Science.* 2016;353(6295):141-144.
17. Hong AN, Yang H, Bu X, Feng P. Pore space partition of metal-organic frameworks for gas storage and separation. *EnergyChem.* 2022;4(4):100080.
18. Wang L, Sun W, Duttwyler S, Zhang Y. Efficient adsorption separation of methane from CO₂ and C₂-C₃ hydrocarbons in a microporous closo-dodecaborate [B₁₂H₁₂]²⁻ pillared metal-organic framework. *J Solid State Chem.* 2021;299:122167.
19. Jiang Y, Hu Y, Luan B, et al. Benchmark single-step ethylene purification from ternary mixtures by a customized fluorinated anion-embedded MOF. *Nat Commun.* 2023;14:401.
20. Gu C, Liu J, Sholl DS. High-throughput screening of anion-pillared metal-organic frameworks for the separation of light hydrocarbons. *J Phys Chem C.* 2021;125(36):20076-20086.
21. Chen X, Li G, Xiao S, Xue W, Zhao X, Yang Q. Efficient capture of Th(IV) and U(VI) by radiation-resistant oxygen-rich ion traps based on a metal-organic framework. *ACS Appl Mater Interfaces.* 2023;15(20):25029-25040.
22. Di Z, Liu C, Pang J, et al. Cage-like porous materials with simultaneous high C₂H₂ storage and excellent C₂H₂/CO₂ separation performance. *Angew Chem Int Ed.* 2021;60(19):10828-10832.
23. Dong Q, Huang Y, Wan J, et al. Confining water nanotubes in a Cu₁₀O₁₃-based metal-organic framework for propylene/propane separation with record-high selectivity. *J Am Chem Soc.* 2023;145(14):8043-8051.
24. Han S, Kim J. Design and screening of metal-organic frameworks for ethane/ethylene separation. *ACS Omega.* 2022;8(4):4278-4284.
25. Jia T, Gu Y, Huang H, Wang L, Li F. Pore-structure control in ultramicroporous porous coordination polymers for efficient selective capture of acetylene. *Sep Purif Technol.* 2023;318:123976.
26. Liu D, Pei J, Zhang X, et al. Scalable green synthesis of robust ultramicroporous Hofmann clathrate material with record C₃H₆ storage density for efficient C₃H₆/C₃H₈ separation. *Angew Chem Int Ed.* 2023;62(12):e202218590.
27. Suo X, Pan H, Chen L, Cui X, Xing H. Control of functionalized pore environment in robust ionic ultramicroporous polymers for efficient removal of trace propyne from propylene. *ACS Appl Mater Interfaces.* 2021;13(36):42706-42714.
28. Chen Y, Du Y, Wang Y, et al. A stable metal-organic framework with well-matched pore cavity for efficient acetylene separation. *AIChE J.* 2021;67(5):e17152.
29. Xu W, Yaghi OM. Metal-organic frameworks for water harvesting from air, anywhere, anytime. *ACS Cent Sci.* 2020;6(8):1348-1354.
30. Xue C, Zhang Q, Wang J, Huang R, Hao Y, Li X. Alkali-induced self-transferring byproduct strategy for strengthening sustainable synthesis of MOF-199 without waste discharge. *ACS Sustain Chem Eng.* 2020;8(49):17945-17955.
31. Zhang YF, Zhang ZH, Ritter L, et al. New reticular chemistry of the rod secondary building unit: synthesis, structure, and natural gas storage of a series of three-way rod amide-functionalized metal-organic frameworks. *J Am Chem Soc.* 2021;143(31):12202-12211.
32. Ren YB, Xu HY, Gang SQ, Gao YJ, Jing X, Du JL. An ultra-stable Zr(IV)-MOF for highly efficient capture of SO₂ from SO₂/CO₂ and SO₂/CH₄ mixtures. *Chem Eng J.* 2022;431:134057.
33. Zhao Z, Liu Y, Liu X, et al. One-step purification of ethylene from acetylene and carbon dioxide by ultramicroporous carbons. *AIChE J.* 2023;69(6):e18046.
34. He C, Yang H, Fu L. A promising controllable CO₂ capture and separation materials for CO₂/CH₄/H₂ under electric field. *Chin Chem Lett.* 2023;34(5):107581.
35. Mukherjee S, Sharma S, Ghosh SK. Hydrophobic metal-organic frameworks: potential toward emerging applications. *APL Mater.* 2019;7(5):050701.
36. Kobielska PA, Howarth AJ, Farha OK, Nayak S. Metal-organic frameworks for heavy metal removal from water. *Coordin Chem Rev.* 2018;358:92-107.

37. Choe JH, Kim H, Hong CS. MOF-74 type variants for CO₂ capture. *Mater Chem Front*. 2021;5(14):5172-5185.
38. Li XY, Song Y, Zhang CX, Zhao CX, He C. Inverse CO₂/C₂H₂ separation in a pillared-layer framework featuring a chlorine-modified channel by quadrupole-moment sieving. *Sep Purif Technol*. 2021;279:119608.
39. Li J, Huang JY, Meng YX, Li L, Zhang LL, Jiang HL. Zr- and Ti-based metal-organic frameworks: synthesis, structures and catalytic applications. *Chem Commun*. 2023;59(18):2541-2559.
40. Chen KJ, Madden DG, Mukherjee S, et al. Synergistic sorbent separation for one-step ethylene purification from a four-component mixture. *Science*. 2019;366(6462):241-246.
41. Shi Y, Xie Y, Cui H, et al. Highly selective adsorption of carbon dioxide over acetylene in an ultramicroporous metal-organic framework. *Adv Mater*. 2021;33(45):2105880.
42. Si Y, He X, Jiang J, Duan Z, Wang W, Yuan D. Highly effective H₂/D₂ separation in a stable Cu-based metal-organic framework. *Nano Res*. 2021;14(2):518-525.
43. Ye Y, Xie Y, Shi Y, et al. A microporous metal-organic framework with unique aromatic pore surfaces for high performance C₂H₆/C₂H₄ separation. *Angew Chem Int Ed*. 2023;62(21):e202302564.
44. Zheng X, Chen L, Zhang H, et al. Optimized sieving effect for ethanol/water separation by ultramicroporous MOFs. *Angew Chem Int Ed*. 2023;62(10):e202216710.
45. Kitagawa S. Porous materials and the age of gas. *Angew Chem Int Ed*. 2015;54(37):10686-10687.
46. Gao J, Cai Y, Qian X, et al. A microporous hydrogen-bonded organic framework for the efficient capture and purification of propylene. *Angew Chem Int Ed*. 2021;60(37):20400-20406.
47. Geng S, Lin E, Li X, et al. Scalable room-temperature synthesis of highly robust ethane-selective metal-organic frameworks for efficient ethylene purification. *J Am Chem Soc*. 2021;143(23):8654-8660.
48. Huang WH, Ren J, Yang YH, et al. Water-stable metal-organic frameworks with selective sensing on Fe³⁺ and Nitroaromatic explosives, and stimuli-responsive luminescence on lanthanide encapsulation. *Inorg Chem*. 2019;58(2):1481-1491.
49. Lv D, Wu Y, Chen J, et al. Improving CH₄/N₂ selectivity within isomeric Al-based MOFs for the highly selective capture of coal-mine methane. *AiChE J*. 2020;66(9):e16287.
50. Wu H, Yuan Y, Chen Y, et al. Efficient adsorptive separation of propene over propane through a pillar-layer cobalt-based metal-organic framework. *AiChE J*. 2020;66(4):e16858.
51. Lin JM, He CT, Liu Y, et al. A metal-organic framework with a pore size/shape suitable for strong binding and close packing of methane. *Angew Chem Int Ed*. 2016;55(15):4674-4678.
52. Liu J, Xie D, Xu X, et al. Reversible formation of coordination bonds in Sn-based metal-organic frameworks for high-performance lithium storage. *Nat Commun*. 2021;12:3131.
53. Luo F, Yan C, Dang L, et al. UTSA-74: a MOF-74 isomer with two accessible binding sites per metal center for highly selective gas separation. *J Am Chem Soc*. 2016;138(17):5678-5684.
54. Zhang L, Ma LN, Wang GD, Hou L, Zhu Z, Wang YY. A new honeycomb MOF for C₂H₄ purification and C₃H₆ enrichment by separating methanol to olefin products. *J Mater Chem A*. 2022;11(5):2343-2348.
55. Zhang F, Li K, Chen J, et al. Efficient N₂/CH₄ separation in a stable metal-organic framework with high density of open Cr sites. *Sep Purif Technol*. 2022;281:119951.
56. Hu F, Huang P, Di Z, Wu M, Jiang F, Hong M. A robust cage-based framework for the highly selective purification of natural gas. *Chem Commun*. 2019;55(69):10257-10260.
57. Cho KH, Yoon JW, Lee JH, et al. Effect of framework rigidity in metal-organic frameworks for adsorptive separation of ethane/ethylene. *Micropor Mesopor Mater*. 2020;307:110473.
58. Zhang Y, Sun W, Luan B, et al. Topological design of unprecedented metal-organic frameworks featuring multiple anion functionalities and hierarchical porosity for benchmark acetylene separation. *Angew Chem Int Ed*. 2023;62:e202309925.
59. Qazvini OT, Babarao R, Telfer SG. Selective capture of carbon dioxide from hydrocarbons using a metal-organic framework. *Nat Commun*. 2021;12:197.
60. Sholl DS, Lively RP. Exemplar mixtures for studying complex mixture effects in practical chemical separations. *JACS Au*. 2022;2(2):322-327.
61. Zhang Y, Yang L, Wang L, Duttwyler S, Xing H. A microporous metal-organic framework Supramolecularly assembled from a Cu^I Dodecaborate cluster complex for selective gas separation. *Angew Chem Int Ed*. 2019;58(24):8145-8150.
62. Zhang Y, Yang L, Wang L, Cui X, Xing H. Pillar iodination in functional boron cage hybrid supramolecular frameworks for high performance separation of light hydrocarbons. *J Mater Chem A*. 2019;7(48):27560-27566.
63. Xian S, Peng J, Pandey H, Thonhauser T, Wang H, Li J. Robust metal-organic frameworks with high industrial applicability in efficient recovery C₃H₈ and C₂H₆ from natural gas upgrading. *Engineering*. 2023;23:56-63.
64. Jiang Y, Hu J, Wang L, et al. Comprehensive pore tuning in an ultra-stable fluorinated anion cross-linked cage-like MOF for simultaneous benchmark propyne recovery and propylene purification. *Angew Chem Int Ed*. 2022;61(18):e202200947.
65. Liu H, Li B, Zhao Y, et al. Investigation on a Zr-based metal-organic framework (MOF-801) for the high-performance separation of light alkanes. *Chem Commun*. 2021;57(96):13008-13011.
66. Qin LZ, Xiong XH, Wang SH, et al. MIL-101-Cr/Fe-NH₂ for efficient separation of CH₄ and C₃H₈ from simulated natural gas. *ACS Appl Mater Interfaces*. 2022;14(40):45444-45450.
67. Liu Y, Xu Q, Chen L, et al. Hydrogen-bonded metal-nucleobase frameworks for highly selective capture of ethane/propane from methane and methane/nitrogen separation. *Nano Res*. 2022;15(8):7695-7702.
68. Chen Y, Qiao Z, Lv D, et al. Selective adsorption of light alkanes on a highly robust indium based metal-organic framework. *Ind Eng Chem Res*. 2017;56(15):4488-4495.
69. Chen F, Guo K, Huang X, et al. Extraction of propane and ethane from natural gas on ultramicroporous carbon adsorbent with record selectivity. *Sci China Mater*. 2023;66(1):319-326.
70. Li J, Luo X, Zhao N, Zhang L, Huo Q, Liu Y. Two finite binuclear [M₂(μ₂-OH)(COO)₂] (M = Co, Ni) based highly porous metal-organic frameworks with high performance for gas sorption and separation. *Inorg Chem*. 2017;56(7):4141-4147.
71. Zhang M, Xin X, Xiao Z, Wang R, Zhang L, Sun D. A multi-aromatic hydrocarbon unit induced hydrophobic metal-organic framework for efficient C₂/C₁ hydrocarbon and oil/water separation. *J Mater Chem A*. 2017;5(3):1168-1175.
72. Wang B, Lv XL, Lv J, et al. A novel mesoporous hydrogen-bonded organic framework with high porosity and stability. *Chem Commun*. 2019;56(1):66-69.
73. Yuan Y, Wu H, Xu Y, et al. Selective extraction of methane from C₁/C₂/C₃ on moisture-resistant MIL-142A with interpenetrated networks. *Chem Eng J*. 2020;395:125057.

SUPPORTING INFORMATION

Additional supporting information can be found online in the Supporting Information section at the end of this article.

How to cite this article: Chen Y, Jiang Y, Li J, et al. Optimizing the cask effect in multicomponent natural gas purification to provide high methane productivity. *AiChE J*. 2024;70(3):e18320. doi:10.1002/aic.18320